WILEY | Hindawi

Research Article

Unsupervised Anomaly Detection for Glaucoma Diagnosis

Wei Zhou [iD],[1] **Yuan Gao,**[2] **Jianhang Ji,**[1] **Shicheng Li** [iD],[3] **and Yugen Yi** [iD][3]

[1]*School of Computer, Shenyang Aerospace University, Shenyang 110136, China*
[2]*Coast Guard Academy, Naval Aviation University, Yantai 264000, China*
[3]*School of Software, Jiangxi Normal University, Nanchang 330022, China*

Correspondence should be addressed to Yugen Yi; yiyg510@jxnu.edu.cn

With the rapid development of high tech, Internet of Things (IoT) and artificial intelligence (AI) achieve a series of achievements in the healthcare industry. Among them, automatic glaucoma diagnosis is one of them. Glaucoma is second leading cause of blindness in the world. Although many automatic glaucoma diagnosis approaches have been proposed, they still face the following two challenges. First, the data acquisition of diseased images is extremely expensive, especially for disease with low occurrence, leading to the class imbalance. Second, large-scale labeled data are hard to obtain in medical image domain. The aforementioned challenges limit the practical application of these approaches in glaucoma diagnosis. To address these disadvantages, this paper proposes an unsupervised anomaly detection framework based on sparse principal component analysis (SPCA) for glaucoma diagnosis. In the proposed approach, we just employ the one-class normal (nonglaucoma) images for training, so the class imbalance problem can be avoided. Then, to distinguish the glaucoma (abnormal) images from the normal images, a feature set consisting of segmentation-based features and image-based features is extracted, which can capture the shape and textural changes. Next, SPCA is adopted to select the effective features from the feature set. Finally, with the usage of the extracted effective features, glaucoma diagnosis can be automatically accomplished via introducing the T^2 statistic and the control limit, overcoming the issue of insufficient labeled samples. Extensive experiments are carried out on the two public databases, and the experimental results verify the effectiveness of the proposed approach.

1. Introduction

Internet of Things (IoT) techniques are emerging, which are known to be among the most critical sources of data streams that produce massive amounts of data continuously from numerous applications, such as transportation systems, security systems, intrusion systems, and fault detection in industry [1–10]. Among them, anomaly detection has drawn tremendous interest in the past couple of years. Since science and technology play a vital role in the medical department, how to establish an anomaly detection big data analysis model supported by medicine becomes a hot topic.

With the rapid growth of the worldwide population, the count of eye diseases is also increased. Among them, glaucoma is one of the serious eye diseases that can lead to irreversible vision loss [11]. According to the recent report [12], the number of glaucoma patients is predicted to increase to 80 million by 2020 and to 111.8 million by 2040. Since glaucoma can cause blindness, early detection and timely treatment are good ways to slow down the progress, preventing further vision loss [13]. In clinical, ophthalmologists always employ the color fundus images to assess the optic nerve head (ONH) for diagnosing glaucoma [14] due to its low cost. Figure 1 depicts the structure of ONH, in which the optic disc (OD) appears as a bright yellowish elliptical region consisting of the central bright region as optic cup (OC) and a peripheral region as the neuroretinal rim. Since ONH assessment requires the qualified ophthalmologists to delineate the OC and OD, it is subjective, labor-intensive, time-consuming, and not suitable for population screening [15].

For large-scale glaucoma screening, it is necessary to use automatic ONH assessment approaches. Since the glaucoma caused by the enlargement OC, several quantitative indicators are presented to identify the symptoms of glaucoma
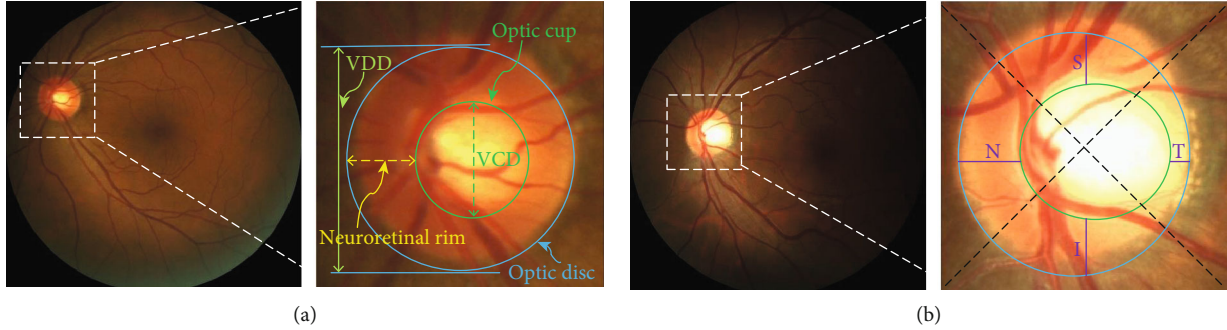
FIGURE 1: The structures of the optic nerve head. (a) Normal, (b) glaucoma.

from the fundus images, such as vertical cup to disc ratio (CDR), disc diameter, rim area, and the ISNT (inferior (I), superior (S), nasal (N), and temporal (T)) rule [16, 17] (as shown in Figure 1). Among these indicators, CDR is well accepted and widely employed indicator by clinicians. The CDR value can be calculated by the ratio of vertical cup diameter (VCD) to vertical disc diameter (VDD). Normally, a larger CDR value means the higher risk of glaucoma and vice versa. Besides, ISNT rule includes inferior (I), superior (S), nasal (N), and temporal (T) rules, which is used for the detection of glaucoma. For a normal subject, I has the highest value of neuro retinal rim configuration followed by S, N, and T.

With the rapid development of pattern recognition and machine learning, a series of automatic glaucoma diagnosis approaches have been proposed recently [18–25]. Although these approaches can achieve automatic glaucoma diagnosis, there are still two challenges in the practical applications. On one hand, the data acquisition of abnormal images is extremely expensive in medical image domain due to the large variations in appearance of OD. On the other hand, it is a time consuming and tedious task to labeling the medical images by the experienced clinicians. Therefore, the cost of obtaining large-scale labeled medical images is often expensive in clinical. In contrast, collecting a large number of normal data is relatively easy.

As we all know, human are good at distinguishing the abnormal images from the normal images [26]. Inspired by this, this paper designs an automatic approach for glaucoma diagnosis, which just uses the normal images for training model. The main advantages of the proposed approach are given as below:

(1) In order to improve the detection accuracy and reduce the computational cost, the region of interest (ROI) in retinal image is extracted by exploring the OD location with unsupervised boundary extraction and Hough transform

(2) Segmentation-based features and image-based features are extracted from the obtained ROIs to capture the shape and textural changes of the fundus images

(3) To reduce the effects caused by noises and redundancy features, an effective feature set can be selected by combining the elastic net penalty and PCA together

(4) In order to solve the issue of class imbalance, the T^2 statistic and the control limit are designed on the normal images, which can be used to distinguish the abnormal images from the normal images, achieving automatic glaucoma diagnosis

(5) Extensive experiments are carried out on the two public fundus databases, and the experimental results indicate that the proposed approach is effective

The remainder of this paper is arranged as below. Section 2 gives some related works, and then, the proposed approach is introduced in details in Section 3. Next, the experimental results and analyses are presented in Section 4. Finally, the whole work is concluded in brief in Section 5.

2. Related Work

The existing automatic glaucoma diagnosis approaches can be divided into two categories: machine learning- (ML-) based approaches and deep learning- (DL-) based approaches.

2.1. Machine Learning- (ML-) Based Approaches. ML-based glaucoma diagnosis approaches follow a fixed procedure [27], e.g., (1) input an image; (2) preprocessing; (3) feature extraction; and (4) classification (diagnosis). In preprocessing stage, Contrast Limited Adaptive Histogram Equalization (CLAHE) [28] is commonly used to reduce the negative effects caused by noise and artifact, improving the quality of the fundus images. In feature extraction stage, a series of important and distinctive hand-crafted features will be extracted to explore the concealed pixel variations in the retinal images. The extracted hand-crafted features are classified into wavelet decomposition-based features [29], morphological-based features [30], nonlinear-based features [31], textural-based features [32], and image descriptor-based features [33]. After feature extraction, the last process is classification. Usually, with the usage of the extracted features, a classification model can be trained which identifies the normal class versus abnormal class. Many classifiers have been employed to distinguish the two classes based on the extracted features, for instance, artificial neural network (ANN) [34], K-nearest neighbor (KNN) [32], support vector machine (SVM) [35], least square support vector machine

(LS-SVM) [29], and extreme learning machine (ELM) [36]. A major challenge in the machine learning-based approaches is that the hand-crafted appropriate features should be set beforehand. Seen from these extracted features, most of them belong to the image-based features. Nevertheless, segmentation-based features are ignored, which can be regarded as one of the most important clinical indicators for glaucoma diagnosis. Besides, usually, the number of normal images is much larger than the abnormal images, leading to the class imbalance. Under this circumstance, the classifier of machine learning approaches can hardly train well, which will affect the final diagnosis performance.

2.2. Deep Learning- (DL-) Based Approaches. DL-based approaches follow the same sequence as ML approaches for glaucoma diagnosis. However, the major difference between them is the deep learning network can self-learn during the training of the network, without extracting a series of hand-crafted features for classification. For example, convolutional neural network (CNN) is the most commonly employed form of deep learning. Generally, a structure of CNN contains (1) convolutional layers, (2) pooling layers, and (3) fully connected layers. The convolutional layer is used to extract the nonlinear features. The pooling layer is utilized to reduce the space dimensionality of sample and keep the important information unchanged. The fully connected layer is to connect the every neuron in the previous layer with the neurons in the current layer of the CNN model. Furthermore, some variations of DL, e.g., adversarial learning [37], FCNs [38], and modified U-net [24], are used to glaucoma diagnosis, improving the diagnosis performance.

Although DL-based approaches have achieved many breakthroughs in medical image analysis, these approaches mainly rely on large-scale labeled data. However, in medical image domain, the samples are always small-scale and unlabeled, so DL-based approaches can hardly perform well [39, 40].

3. Our Approach

Our approach consists of the following three stages, including ROI extraction, features extraction (segmentation-based features and image-based features), and glaucoma diagnosis. The flowchart of the proposed approach is shown in Figure 2.

3.1. ROI Extraction. Generally, the resolution of original fundus image is relatively large. Meanwhile, the region of interest for glaucoma diagnosis is just a small region according to the clinical prior knowledge. In order to reduce the influence of the unnecessary background information and the computation cost, improving the diagnosis accuracy, the extraction of ROI around the OD is necessary (as shown in Figure 3).

The process of ROI extraction consists of the following three stages: first, this paper employs our previous proposed approach named as an adaptive rough OD boundary curve extraction based on unsupervised learning [16] to extract the OD region (as shown in Figure 3(b)). After that, in order to accurately locate the center of OD, the Circular Hough Transform (CHT) is employed to the extracted OD region

according to the fact that the prior knowledge of OD is circle in shape, depicted in Figure 3(c). At last, with the usage of the extracted center of OD as the ROI center, according to the clinical experience [16], this paper cuts the original images into small images with the resolution of 400×400 on the REFUGE and RIM-ONE r2 databases, which are called ROIs around the OD. An example from the REFUGE database is shown in Figure 3(d).

Successful optic disc center localization is considered to be that the distance between the estimated optic disc center and the manually selected center is less than the optic disc radius [41, 42]. Compared with the state-of-the-art OD detection approaches, our approach is more robust to the image quality, contrast, brightness, and different lesions. Since human vision is more sensitive to green color, only green channel of ROI is extracted from the RGB image for further processing. Meanwhile, CLAHE is introduced into the extracted green channel of ROI [28] to enhance the contrast (illustrated in Figure 3(e)).

3.2. Feature Extraction. OD with varying intrinsic principal features, e.g., distinct vessel structures, sizes, and brightness, gives more challenges for glaucoma diagnosis. To fully explore the difference between the normal images and abnormal images, improving the effectiveness and accuracy of the glaucoma diagnosis, this paper describes the OD from the following two sides. For one side, inspired by the clinical glaucoma diagnosis, a series of segmentation-based features are extracted to accurately capture the shape deformations to characterize glaucoma. For another, some image-based features are extracted to capture the shape and textual changes in OD. We believe that taking the segmentation-based and image-based features into a united framework can provide complementary and independent information for OD descriptions. The detailed descriptions of the extracted features are given as below.

3.2.1. Extraction of Segmentation-Based Features. Based on the extracted ROI around the OD, this paper adopts [11] to segment the OD and OC. In clinical, for a normal fundus image, the rim is the thickest in the inferior (I) sector and thinnest in the temporal (T) sector (as shown in Figure 1). Usually, experienced ophthalmologists observe inferior (I), superior (S), nasal (N), and temporal (T) quadrants for glaucoma diagnosis. Therefore, a series of clinical features are extracted from the segmented OD and OC, denoted as F1 to F5 (as shown in Table 1). F1-F3 are based on rim-disc ratio, and F4-F5 are calculated by rim profile and ISNT, respectively. Among them, the calculation of F5 is based on a disk-shaped region named as the NRR, obtained by removing the OC from the OD.

The calculation process of F5 is given as below: Figure 4(a) is the original image, and Figure 4(f) is the NRR. The masks employed in this paper are used to measure the NRR in each quadrant which are depicted in Figures 4(b)–4(e). The NRR area in superior, nasal, inferior, and temporal are, respectively, shown in Figures 4(g)–4(j), which can be used to calculate F5.
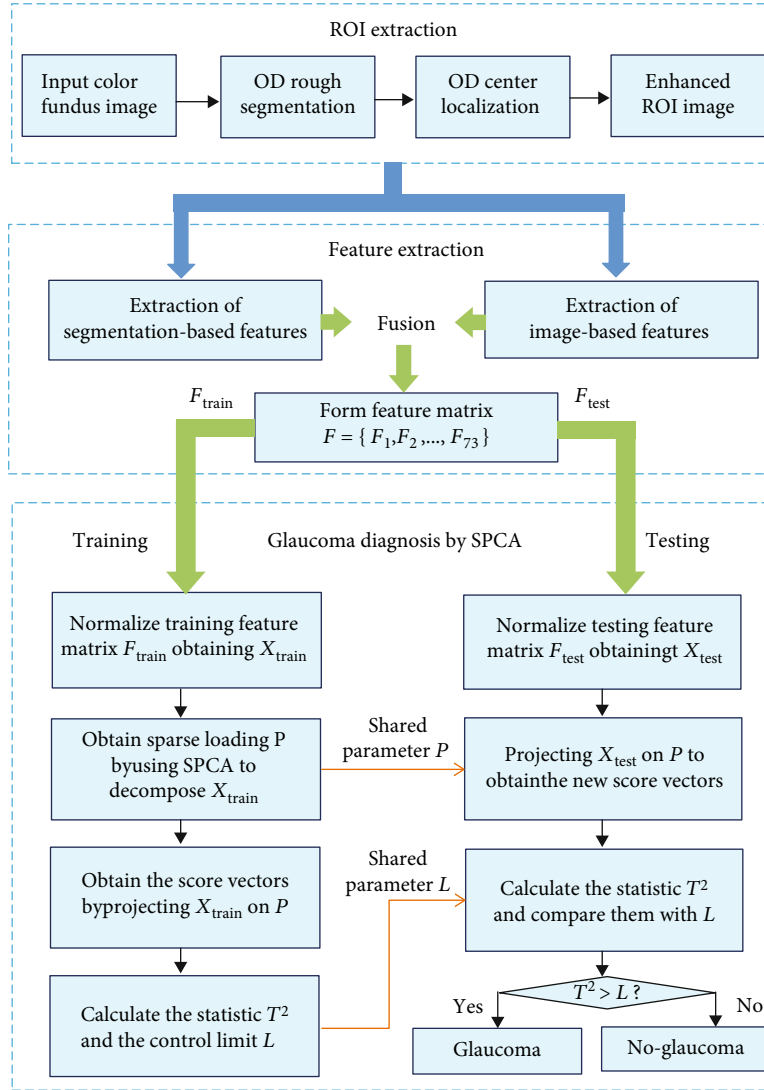
Figure 2: The flowchart of the proposed approach.

3.2.2. Extraction of Image-Based Features. Since the gray level of the image on the edge is discontinuous, it has singularity. Recent studies have shown that the multiresolution features of wavelet coefficients and the localization characteristics of wavelet analysis can be used to obtain the domain features at different scales. In addition, the high frequency information decomposed by wavelet can also be used for multiscale edge detection [43], which is very fit for medical image processing and analysis. Inspired by the advantages of wavelet features, this paper employs an adaptive signal decomposing approach, named as two-dimensional (2D) EWT with Littlewood-Paley as an empirical wavelet [44] to decompose the image into various frequency bands. Based on the decomposed components of (2D) EWT, a series of image-based features consisting of chip histogram, gray level cooccurrence matrix (GLCM), and moment invariance are extracted. Here, the enhanced green channel image is utilized as the input of (2D) EWT. For each input image, four frequency bands can be decomposed. The detailed image-based features descriptions are given as below:

(a) Chip histogram features

Chip feature belongs to statistical textural feature, which can be extracted from the second-order histogram. There are six features in it including mean, variance, skewness, kurtosis, energy, and entropy. For a given gray image, $t(i)$ is the probability density function of the intensity level i, which is denoted as $t(i) = \text{Histogram}(i)/T$, $i = 1, 2, 3, \cdots, N$. T is the total pixels in the gray image, and N is the total number of gray levels, in which Q is the gray level vector represented as $[1, 2, 3, \cdots, N]$. The expressions of the chip histogram features are depicted in Table 2.

(b) GLCM features

GLCM is utilized to extract the texture in an image by doing the transition of gray level between two pixels, which is one of the earliest approaches for texture feature extraction [45]. For each GLCM, four directions can be computed, in which each direction has four different characteristics, i.e.,
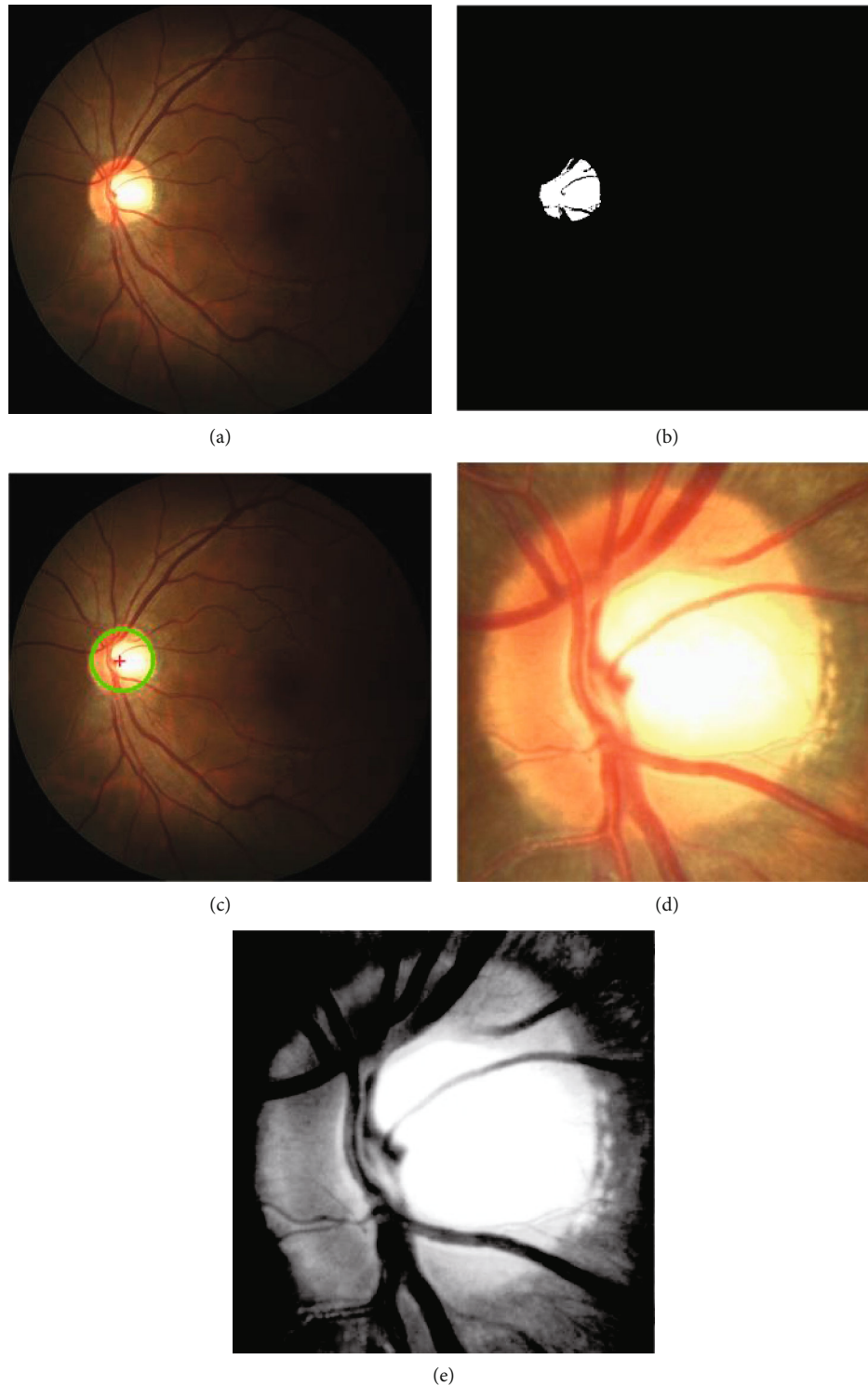
Figure 3: (a) Original image; (b) coarse segmentation image; (c) OD localization-based CHT; (d) extracted ROI; (e) enhanced green channel image by CLAHE.

correlation, contrast, energy, and homogeneity. For each characteristic, we extract the mean value of four different directions. Therefore, there are four GLCM features for each image. Suppose that $G(u, v)$ denotes (u, v) entries in normalized GLCM, and the mean and standard deviation along u and v coordinates are expressed as (μ_x and μ_y) and (σ_x and σ_y), respectively. Table 3 gives the expressions of the GLCM features.

(c) Moment Invariance features

TABLE 1: Extraction of segmentation-based features and the corresponding expressions.

Segmentation-based features	Expressions
F1: vertical CDR	vCDR = VCD/VDD
F2: the area ratio of rim to disc	Area_ratio = Rim_Area/OD_Area
F3: the major axis length of OD	Length_Major_axis_OD = L_OD
F4: the area of rim	OD_Area − OC_Area
F5: neuro-retinal rim (NRR)	NRR in I quardrant area + NRR in S quardrant area/NRR in N quardrant area + NRR in T quardrant area

In order to overcome the changes of object shape, position, and orientation [46], this paper employs the moment invariance features for describing the OD and OC. There are seven features in moment invariant features, and the mathematical expressions of these features are shown in Table 4.

The invariants λ_{mn} can be calculated by $\lambda_{mn} = \mu_{mn}/\mu_{00}^{1+(m+n)/2}$, in which μ_{mn} and μ_{00} are, respectively, denoted as the center moment and the zeroth central moment.

After feature extraction, 73 features in which 5 segmentation-based features and 68 $4 \times (6 + 4 + 7)$ image-based features are computed for each input image, forming a 73-dimension feature set $F = \{F_1, F_2, \cdots, F_{73}\}$. Each feature F_i is normalized to zero mean and unit variance by using $F_i' = (F_i - \mu_i)/\sigma_i$ in which μ_i is the mean of the ith feature, and σ_i is the corresponding standard deviation.

3.3. Anomaly Detection for Glaucoma with SPCA. In this subsection, we firstly review the (principal component analysis, PCA) and sparse PCA. Then, T^2 statistic of glaucoma and the corresponding control limit are given for glaucoma diagnosis.

3.3.1. PCA. PCA is one of the most popular dimensionality reduction approaches, which is aimed at maximizing the variance of projections on the new directions. For PCA, a series of load vectors can be constructed by the orthogonal vectors. Supposing that $X \in R^{N \times D}$ is a given training sample set, N and D denote the number of the samples and variables (features), respectively. The objective function of PCA is given as

$$\max_{u \neq 0} \frac{u^T X^T X u}{u^T u}, \tag{1}$$

where $u \in R^D$. The solution of Equation (1) can be computed by singular value decomposition (SVD) as

$$\frac{1}{\sqrt{N-1}} X = W \Sigma U^T, \tag{2}$$

where $W \in R^{N \times N}$ and $U \in R^{D \times D}$ are unitary matrices, in which the orthogonal column vectors in matrix U are called the load vectors. Projecting X on the ith column has the variance as σ_i^2. $\Sigma \in R^{N \times D}$ is a diagonal matrix where the elements in main diagonal are the nonnegative singular values in descending order $(\sigma_1 \geq \sigma_2, \cdots, \geq \sigma_{\min (N,D)} \geq 0)$, and the others are zeros.

A new load matrix $P \in R^{D \times A}$ can be obtained by selecting the first A columns in U, named as the principal component subspace (PCS), which is represented as $T = XP$. For a given new sample x, it can be projected on the PCS as

$$t = P^T x \in \text{PCS}, \tag{3}$$

In Equation (3), A is a parameter, which is calculated by cumulative percent variance (CPV), and this paper adopts reference [47] to resolve it.

3.3.2. Sparse PCA. Seen from the PCA, its major work is to acquire the maximum variance on the certain loading vectors. However, in practice, some principal components are linear relevant with each other and some of them have large noises, which will weaken the precision of detection. Inspired by the advantages of sparsity, sparse PCA has been proposed by performing the maximization of objective function under the L1 norm constraint as

$$\sum_{j=1}^{D} |u_j| \leq s, \tag{4}$$

where s is the number of nonzero elements in a load vector. $u_j (j \in \{1, 2, \cdots, D\})$ denotes the jth element of the load vector. By introducing the aforementioned sparse constraint, each principle component has lesser original variables. Therefore, it not only enhances the interpretability of the principal components but also reduces the storage space.

Many approaches have been designed to solve Equation (4). Among them, Jolliffe and Uddin [48] proposed the most effective approach to resolve it. The main processes are depicted as below: first, PCA can be recast exactly by a regression problem, such as ridge regression. Then, the regression problem is changed to an elastic-net regression by introducing the L1 norm constraint. For more details, please refer to reference [49].

3.3.3. Index and Control Limit. A series of statistics have been applied to multivariable statistical analysis. Among them, one of the most preventative ways, namely, Hotelling's T^2 statistic, is utilized to represent the variability in the PCS, which is defined as

$$T^2 = x^T P \Lambda^{-1} P^T x, \tag{5}$$
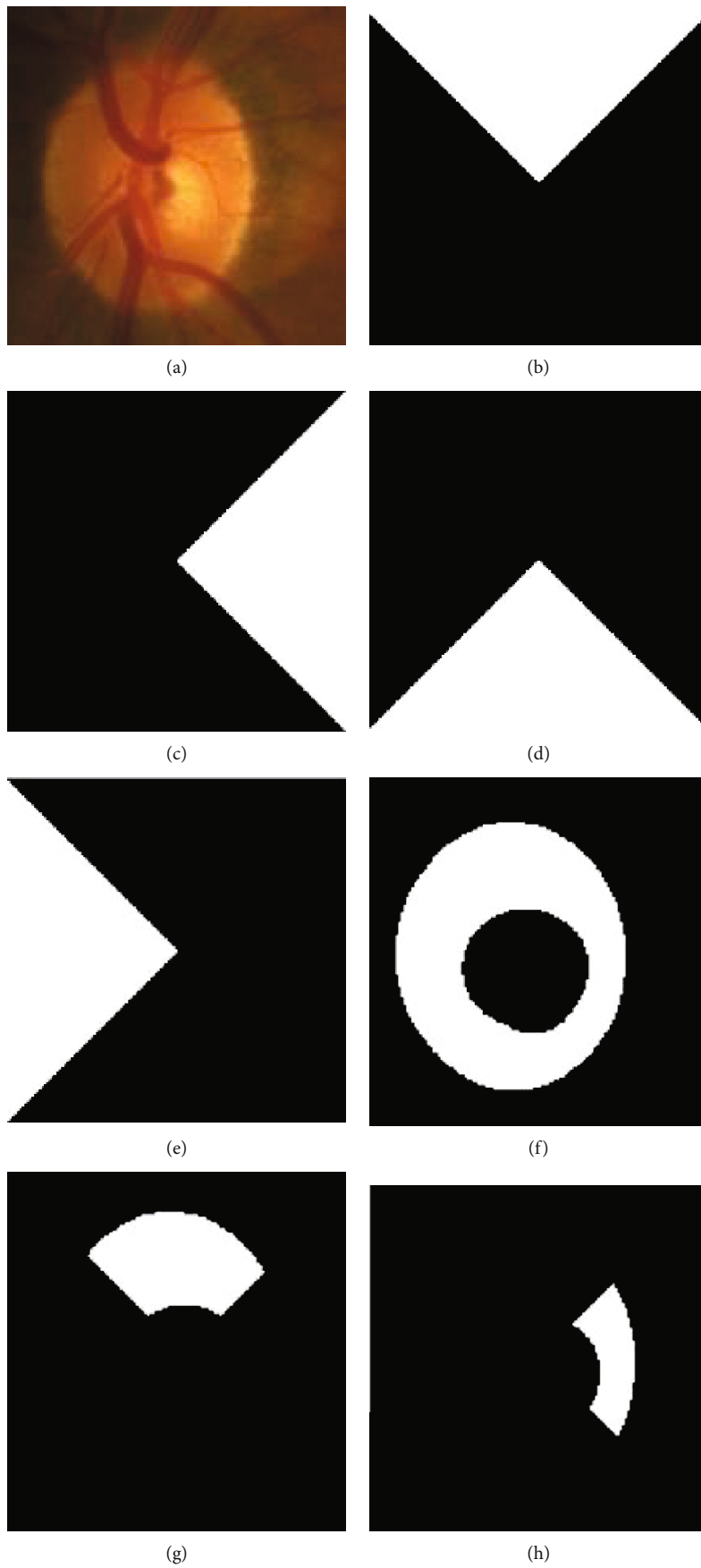
(a)

(b)

(c)

(d)

(e)

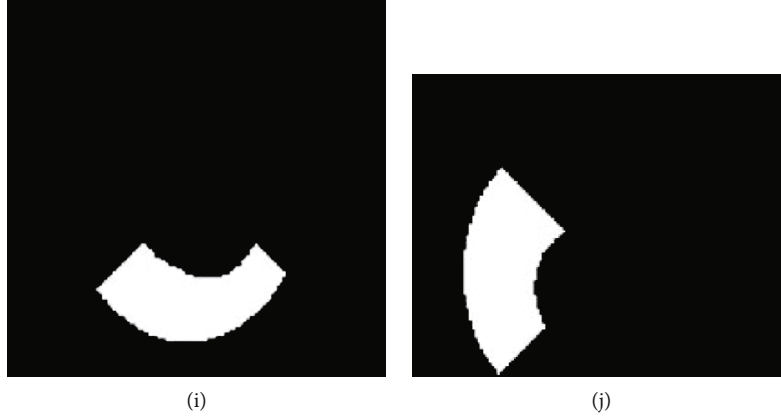(f)

(g)

(h)

Figure 4: Continued.

FIGURE 4: (a) Original color fundus image; (b–e) the masks in superior, nasal, inferior, and temporal, respectively. (f) NRR; (g–j) NRR in superior, nasal, inferior, and temporal, respectively.

TABLE 2: Expressions of chip histogram features.

Chip histogram features	Expressions
Mean	$\sum_{i=1}^{N}\left(t(i) \times Q(i)\right)$
Variance	$\sum_{i=1}^{N}\left(t(i) \times Q(i)^2\right)$
Skewness	$\left[\sum_{i=1}^{N}\left(t(i) \times Q(i) - \text{Mean}\right)^3\right] \times \left[\left(\sqrt{\text{Variance}}\right)^{-3}\right]$
Kurtosis	$\left[\sum_{i=1}^{N}\left(t(i) \times Q(i) - \text{Mean}\right)^4\right] \times \left[\left(\sqrt{\text{Variance}}\right)^{-4}\right]$
Energy	$\sum_{i=1}^{N} t(i) \times t(i)$
Entropy	$-\sum_{i=1}^{N} t(i) \times \log t(i)$

TABLE 3: Expressions of GLCM feature.

GLCM features	Expressions
Contrast	$\sum_{u=1}\sum_{v=1}(u-v)^2 \times G(u,v)$
Correlation	$\sum_{u=1}\sum_{v=1} uv \times G(u,v) - \mu_x\mu_y/\sigma_x\sigma_y$
Energy	$\sum_{u=1}\sum_{v=1} G(u,v)^2$
Homogeneity	$\sum_{u=1}\sum_{v=1} G(u,v)/1 + (u-v)^2$

where $\Lambda = \Sigma^T \Sigma$. The sample vector x follows a multivariate normal distribution.

$$\frac{N(N-A)}{A(N^2-1)} T^2 \sim F_{A,N-A}, \qquad (6)$$

where $F_{A,N-A}$ is an F distribution with A and $N-A$ degrees of freedom. For a given significance level α, the detected image is regarded as glaucoma if

$$T^2 \leq T_\alpha^2 \equiv \frac{A(N^2-1)}{N(N-A)} F_{A,N-A;A}. \qquad (7)$$

The whole process of the proposed glaucoma diagnosis approach can be divided into the following four stages. In the first stage, an unsupervised boundary curve extraction model and Circular Hough Transform (CHT) are used to extract ROI. In the second stage, a series of features containing segmentation-based and image-based features are extracted from the ROI, forming the feature matrix. The third stage is the offline training. In this part, the glaucoma model is constructed based on spares PCA, and the control limit L is also given. The last stage is the online testing. For a new fundus image, first, repeat the process of stages one and two, and then, compute the corresponding statistic; at last, compare them with the control L for distinguishing glaucoma from normal.

4. Experiments and Results

4.1. Databases. In experiment, we employ two public databases to verify the effectiveness of the proposed approach. The detailed descriptions of the databases are given as below:

Retinal Fundus Glaucoma Challenge (REFUGE) database [50] consists of 1200 color retinal fundus images stored in JPEG format, in which 120 are glaucomatous and 1080 are nonglaucoma images. REFUGE database is divided into three parts: 400 training images, 400 validation images, and 400 testing images, in which 400 training images are acquired with a Zeiss Visucam 500 fundus camera with the resolution of 2124×2056 pixels, and the 400 validation images and 400 testing images are acquired with Canon CR-2 device with the resolution of 1634×1634 pixels. In REFUGE database, only 400 training images and 400 validation images which are labeled as "ground truth" with the segmentation results of OD and OC and the rest 400 testing images without labeling the ground truth. Therefore, in this experiment, we adopt 400 training images (40 glaucoma images and 360 nonglaucoma images) and 400 validation images (40 glaucoma images and 360 nonglaucoma images)

Table 4: Expressions of moment invariance features.

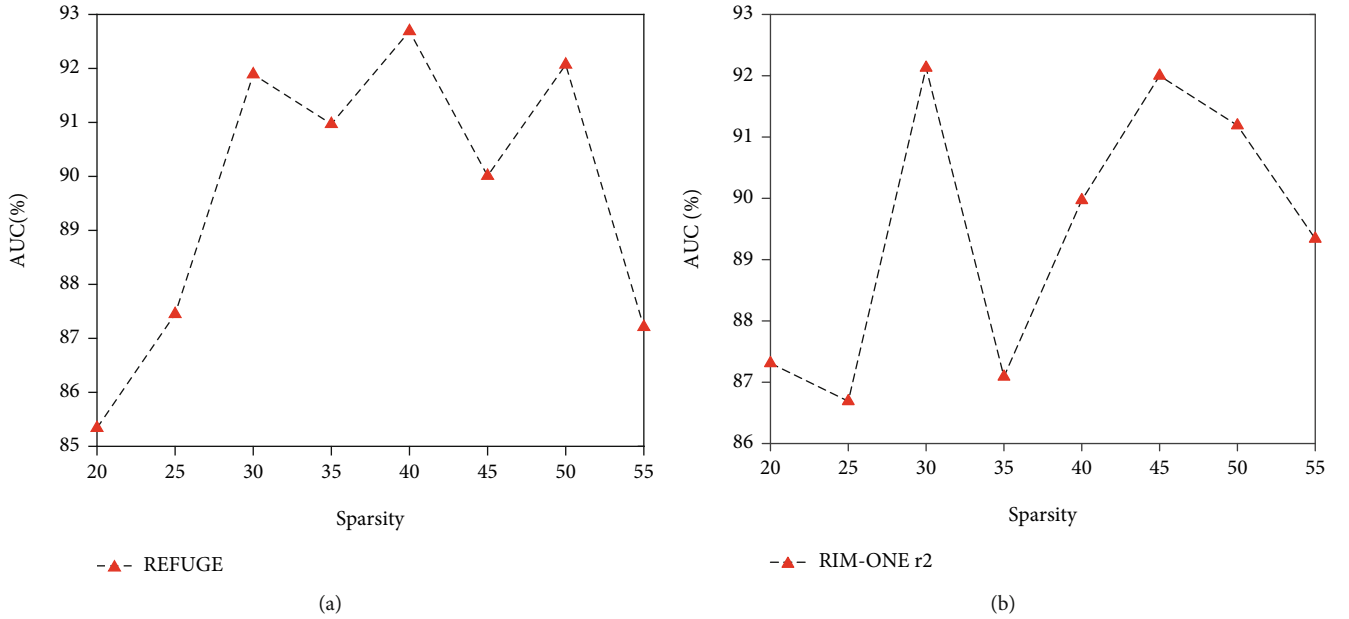| Moment invariance features	Expressions
MV1	$\lambda_{20} + \lambda_{02}$
MV2	$(\lambda_{20} - \lambda_{02})^2 + 4\lambda_{11}^2$
MV3	$(\lambda_{30} - 3\lambda_{12})^2 + (3\lambda_{21} - \lambda_{03})^2$
MV4	$(\lambda_{30} + \lambda_{12})^2 + (\lambda_{21} + \lambda_{03})^2$
MV5	$(\lambda_{30} - 3\lambda_{12})(\lambda_{30} + \lambda_{12})\big((\lambda_{30} + \lambda_{12})^2 - 3(\lambda_{21} + \lambda_{03})^2\big)$ $+ (3\lambda_{21} - \lambda_{03})(\lambda_{21} + \lambda_{03})\big(3(\lambda_{30} + \lambda_{12})^2 - (\lambda_{21} + \lambda_{03})^2\big)$
MV6	$(\lambda_{20} - \lambda_{02})\big[(\lambda_{30} + \lambda_{12})^2 - (\lambda_{21} + \lambda_{03})^2\big] + 4\lambda_{11}(\lambda_{30} + \lambda_{12})(\lambda_{21} + \lambda_{03})$
MV7	$(3\lambda_{21} - \lambda_{03})(\lambda_{30} + \lambda_{12})\big[(\lambda_{30} + \lambda_{12})^2 - 3(\lambda_{21} + \lambda_{03})^2\big] - (\lambda_{30} - 3\lambda_{12})$ $(\lambda_{21} + \lambda_{03})\big[3(\lambda_{30} + \lambda_{12})^2 - (\lambda_{21} + \lambda_{03})^2\big]$

Figure 5: The classification performance (AUC) with different values of sparsity on the REFUGE and RIM-ONE r2 databases. (a) REFUGE database, (b) RIM-ONE r2 database.

to train and verify the effectiveness of the proposed approach. In total, there are 80 glaucoma images and 720 nonglaucoma images. In experiment, 500 nonglaucoma images are randomly selected constructing the training set. 20 glaucoma images and 160 nonglaucoma images are regarded as the validation set (20 + 160). And the rest 60 nonglaucoma images and 60 glaucoma images are regarded as the testing set (60 + 60). The random sample selection process is repeated 10 times, and the average result is regarded as the final result.

RIM-ONE r2 database [51] comprises of 455 retinal fundus images, in which 255 are normal images and 200 are glaucoma images. In experiment, first, all of the images in this database are resized in the same dimensionality. And then, the ROI extraction depicted in Section 2 is used to these images. At last, a series of features are extracted from the obtained ROIs, which are regarded as the inputs for our approach.

In experiment, 200 nonglaucoma images are randomly selected constructing the training set. 25 glaucoma images and 25 nonglaucoma images are randomly selected as the validation set (25 + 25). The rest 30 nonglaucoma images and 175 glaucoma images are regarded as the testing set (30 + 175). The random sample selection process is repeated 10 times, and the average result is regarded as the final result.

The proposed approach is trained and tested by using a desktop computer having 16 GB random access memory (RAM), Intel ® Core™ i7 CPU950@3.7 GHz. We develop our approach using MATLAB 2021a for training and testing.

4.2. Evaluation Criterion. In order to evaluate the effectiveness of the proposed approach, three evaluation criteria, namely, accuracy, sensitivity, and specificity, are employed
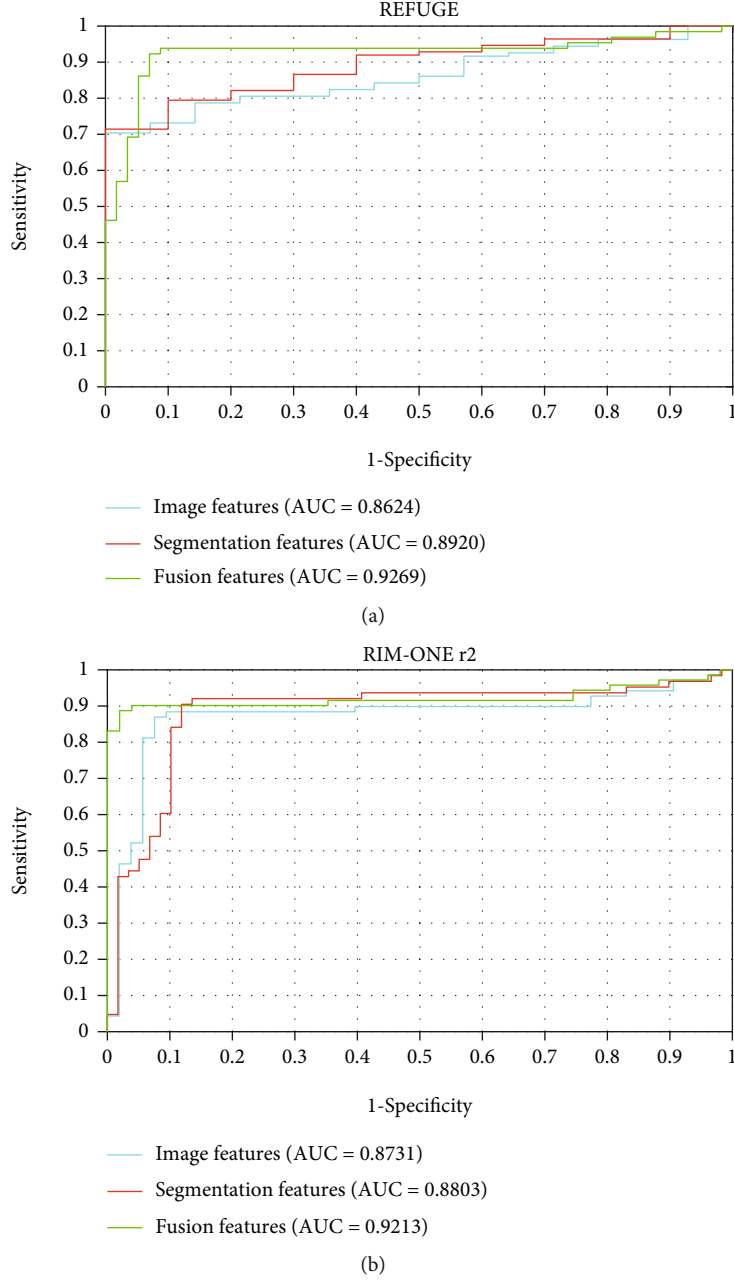
(a)

(b)

FIGURE 6: The ROC curves of the proposed glaucoma diagnosis approach with three different kinds of feature extraction ways on the REFUGE and RIM-ONE r2 databases.

in this experiment. The corresponding mathematical expressions of these evaluation criteria are depicted as below:

$$\text{Accuracy} = \frac{TP + TN}{TP + TN + FP + FN} \times 100\%, \qquad (8)$$

$$\text{Sensitivity} = \frac{TP}{TP + FN} \times 100\%, \qquad (9)$$

$$\text{Specificity} = \frac{TN}{TN + FP} \times 100\%, \qquad (10)$$

where true positive (TP) is the number of glaucoma images that are correctly identified; false negative (FN) is the number of incorrectly found as nonglaucoma images; false positive (FP) is the number of incorrectly found as glaucoma images. true negative (TN) is the number of nonglaucoma images that are correctly identified.

In order to evaluate the effectiveness of the proposed approach, receiver-operating characteristics (ROC) curve is utilized in this paper. In ROC curve, the vertical axis is the sensitivity and the horizontal axis is (1-specificity). The area under the ROC curve denotes as the AUC value

Table 5: Comparison of the proposed approach against the state-of-the-art approaches on the testing set of REFUGE database and RIM-ONE r2 database.

Methods	Accuracy (%) REFUGE	Accuracy (%) RIM-ONE r2
Wavelet features [52]	58.70	59.81
Superpixel segmentation [53]	63.53	78.64
Semisupervised clustering [54]	81.95	82.76
Deep learning [55]	80.12	84.46
AWLCSC [31]	85.54	85.56
Ours	92.44	93.65

for measuring and describing the algorithm performance. A higher AUC indicates that the performance of the approach is better.

4.3. Parameter Settings and Analysis. There are two hyperparameters, i.e., the sparseness criterion for the SPCA stage and the sigma-like threshold on the actual classification stage. Here, sparsity will make principal component coefficients (the coefficients in front of each variable when forming principal components) be sparse. In other words, most of the coefficients will become zero values. In this way, we can highlight the major parts of principal components, so that the principal components will become easier to explain. In order to choose suitable sparstiy, this paper employs the commonly used ROC curve. In our experiment, the validation set is employed for parameter selection and validation. For REFUGE database, 160 nonglaucoma images and 20 glaucoma images construct the validation set. For RIM-ONE r2 database, the validation set consists of 20 nonglaucoma images and 20 glaucoma images.

In our experiment, we tune the values of sparsity parameter by searching the grid {20, 25, 30, 35, 40, 45, 50, 55} for REFUGE and RIM-ONE r2 databases. We test the diagnosis performance (AUC) of the proposed approach under different values of sparsity parameter on the REFUGE and RIM-ONE r2 databases (as depicted in Figures 5(a) and 5(b)). As seen from these figures, we can learn that the proposed glaucoma diagnosis approach can achieve maximum AUC values on the REFUGE and RIM-ONE r2 databases when the values of sparsity are set as 40 and 30. After the sparsity is determined, the threshold for T^2 can be computed by Equation (7).

4.4. Experimental Results and Analysis. In this subsection, we will carry out two experiments to verify the effectiveness of the proposed approach. For one side, the proposed approach with different features including segmentation-based features, image-based features, and their fusion features will be tested, respectively, and the obtained diagnosis performances are shown in Figure 6.

Seen from the results depicted in Figure 6, we can learn that when the proposed approach employs the fusion features, it can achieve the best performance on the testing set. The main reason is that the segmentation-based and image-based features can capture the shape and textural

changes, respectively. Nevertheless, the fusion of these features provides complementary information for glaucoma diagnosis, which can improve diagnosis performance.

For another, the performance of the proposed approach is compared against the state-of-the-art approaches, i.e., wavelet features [52], superpixel segmentation [53], semisupervised clustering [54], deep learning [55], and AWLCSC [31]. Table 5 shows the diagnosis results obtained by different algorithms on the REFUGE database and RIM-ONE r2 database, respectively. Among them, superpixel segmentation, wavelet features, and deep learning are supervised learning approaches; semisupervised clustering is the semisupervised learning approach; AWLCSC and the proposed approach belong to unsupervised learning approaches. For supervised learning approaches, they can achieve good performance when a large number of labeled samples are used to train model. However, a large number of labeled data are hard to obtain, especially for medical domain. Under this situation, semisupervised learning and unsupervised learning have gained tremendous attention. Although these approaches can overcome the problem of insufficient samples, the class imbalance problem still lies in these approaches reducing their classification performance. Different from the existing glaucoma diagnosis approaches, this paper just employs one-class normal data for constructing model and designs the control limit for detecting the abnormal data. Therefore, the aforementioned two limitations can be avoided. According to the comparison results depicted in Table 5, we can learn that the proposed approach is more reliable than other tested approaches in terms of diagnosis accuracy, indicating the effectiveness of the proposed approach.

5. Conclusions

In this paper, we propose an unsupervised anomaly detection approach via sparse PCA for glaucoma diagnosis. Since the ODs vary in sizes, shapes, and appearances for glaucoma images, it can hardly construct an effective model to diagnose glaucoma. Instead of using the glaucoma images, this paper just constructs the diagnosis model based on the nonglaucoma images. Therefore, the proposed approach overcomes the class imbalance issue, which is a hard problem in classification. Furthermore, a series of features including segmentation-based features and image-based features are designed, which can capture the shape and textural changes, respectively, improving the discrimination of the OD and OC. Experimental results indicate that the proposed approach can achieve good glaucoma diagnosis performance.

The main disadvantage of the proposed approach is that the fundus images were obtained by different equipment and institutions, so that the trained model parameters by our proposed approach cannot perform stable detection results. Therefore, it is necessary to improve the generalization of the model from different datasets, which is one of our future research directions. Besides, more large-size databases will be introduced to further verify the effectiveness of the proposed approach.

Data Availability

The data are derived from public domain resources.

Conflicts of Interest

The authors declare that they have no conflicts of interest.

Acknowledgments

References

[1] F. Zhu, J. Yang, C. Gao, S. Xu, N. Ye, and T. Yin, "A weighted one-class support vector machine," *Neurocomputing*, vol. 189, pp. 1–10, 2016.

[2] Y. He, G. Duan, G. Luo, and X. Liu, "Robust visual relationship detection towards sparse images in Internet-of-Things," *Wireless Communications and Mobile Computing*, vol. 2021, 10 pages, 2021.

[3] F. Zhu, Y. Ning, X. Chen, Y. Zhao, and Y. Gang, "On removing potential redundant constraints for SVOR learning," *Applied Soft Computing*, vol. 102, p. 106941, 2021.

[4] Y. Yi, W. Zhou, Y. Shi, and J. Dai, "Speedup two-class supervised outlier detection," *IEEE Access*, vol. 6, pp. 63923–63933, 2018.

[5] Z. Zhang, H. Chen, X. Yin, and J. Deng, "EAWNet: an edge attention-wise objector for real-time visual Internet of Things," *Wireless Communications and Mobile Computing*, vol. 2021, 15 pages, 2021.

[6] F. Zhu, N. Ye, W. Yu, S. Xu, and G. Li, "Boundary detection and sample reduction for one-class support vector machines," *Neurocomputing*, vol. 123, pp. 166–173, 2014.

[7] W. Zhou, Z. Gong, W. Guo, N. Han, and S. Qiao, "Robust graph structure learning for multimedia data analysis," *Wireless Communications and Mobile Computing*, vol. 2021, 12 pages, 2021.

[8] Y. Yi, Y. Shi, W. Wang, G. Lei, J. Dai, and H. Zheng, "Combining boundary detector and SND-SVM for fast learning," *International Journal of Machine Learning and Cybernetics*, vol. 12, no. 3, pp. 689–698, 2021.

[9] S. Li, Q. Liu, J. Dai, W. Wang, X. Gui, and Y. Yi, "Adaptive-weighted multiview deep basis matrix factorization for multimedia data analysis," *Wireless Communications and Mobile Computing*, vol. 2021, 12 pages, 2021.

[10] R. Al-amri, R. K. Murugesan, M. Man, A. F. Abdulateef, M. A. Al-Sharafi, and A. A. Alkahtani, "A review of machine learning and deep learning techniques for anomaly detection in IoT data," *Applied Sciences*, vol. 11, no. 12, p. 5320, 2021.

[11] W. Zhou, Y. Yi, Y. Gao, and J. Dai, "Optic disc and cup segmentation in retinal images for glaucoma diagnosis by locally statistical active contour model with structure prior," *Computational and Mathematical Methods in Medicine*, vol. 2019, 16 pages, 2019.

[12] Y.-C. Tham, X. Li, T. Y. Wong, H. A. Quigley, T. Aung, and C.-Y. Cheng, "Global prevalence of glaucoma and projections of glaucoma burden through 2040: a systematic review and meta-analysis," *Ophthalmology*, vol. 121, no. 11, pp. 2081–2090, 2014.

[13] L. Li, M. Xu, H. Liu et al., "A large-scale database and a CNN model for attention-based glaucoma detection," *IEEE Transactions on Medical Imaging*, vol. 39, no. 2, pp. 413–424, 2020.

[14] H. Fu, J. Cheng, Y. Xu, D. W. K. Wong, J. Liu, and X. Cao, "Joint optic disc and cup segmentation based on multi-label deep network and polar transformation," *IEEE Transactions on Medical Imaging*, vol. 37, no. 7, pp. 1597–1605, 2018.

[15] R. Zhao, X. Chen, and X. Liu, "Direct cup-to-disc ratio estimation for glaucoma screening via semi-supervised learning," *IEEE Journal of Biomedical and Health Informatics*, vol. 24, no. 4, pp. 1104–1113, 2020.

[16] Y. GAO, W. U. Chengdong, Y. U. Xiaosheng, W. ZHOU, and W. U. Jiahui, "Full-automatic optic disc boundary extraction based on active contour model with multiple energies," *IEICE Transactions on Fundamentals of Electronics, Communications and Computer Sciences*, vol. E101.A, no. 3, pp. 658–661, 2018.

[17] J. Guo, G. Azzopardi, C. Shi, N. M. Jansonius, and N. Petkov, "Automatic determination of vertical cup-to-disc ratio in retinal fundus images for glaucoma screening," *IEEE Access*, vol. 7, pp. 8527–8541, 2019.

[18] A. Aquino, M. E. Gegúndez-Arias, and D. Marín, "Detecting the optic disc boundary in digital fundus images using morphological, edge detection, and feature extraction techniques," *IEEE Transactions on Medical Imaging*, vol. 29, no. 11, pp. 1860–1869, 2010.

[19] B. Dashtbozorg, A. M. Mendonça, and A. Campilho, "Optic disc segmentation using the sliding band filter," *Computers in Biology and Medicine*, vol. 56, pp. 1–12, 2015.

[20] A. Chakravarty and J. Sivaswamy, "Joint optic disc and cup boundary extraction from monocular fundus images," *Computer Methods and Programs in Biomedicine*, vol. 147, pp. 51–61, 2017.

[21] Y. Zheng, D. Stambolian, and J. O'Brien, *Optic Disc and Cup Segmentation from Color Fundus Photograph Using Graph Cut with Priors, in Proceedings of the International Conference on Medical Image Computing and Computer-Assisted Intervention*, Springer, Berlin, Heidelberg, 2013.

[22] J. Zilly, J. M. Buhmann, and D. Mahapatra, "Glaucoma detection using entropy sampling and ensemble learning for automatic optic cup and disc segmentation," *Computerized Medical Imaging and Graphics*, vol. 55, pp. 28–41, 2017.

[23] K. K. Maninis, J. Pont-Tuset, and P. Arbeláez, "Deep retinal image understanding," in *in: International Conference on Medical Image Computing and Computer-Assisted Intervention*, pp. 140–148, Springer, Cham, 2016.

[24] A. Sevastopolsky, "Optic disc and cup segmentation methods for glaucoma detection with modification of U-Net

convolutional neural network," *Pattern Recognition and Image Analysis*, vol. 27, no. 3, pp. 618–624, 2017.

[25] S. M. Shankaranarayana, K. Ram, and K. Mitra, "Joint optic disc and cup segmentation using fully convolutional and adversarial networks," in *Fetal, Infant and Ophthalmic Medical Image Analysis*, pp. 168–176, Springer, Cham, 2017.

[26] W. Zhou, C. Wu, D. Chen, Y. Yi, and W. Du, "Automatic microaneurysm detection using the sparse principal component analysis-based unsupervised classification method," *IEEE Access*, vol. 5, pp. 2563–2572, 2017.

[27] A. Sarhan, J. Rokne, and R. Alhajj, "Glaucoma detection using image processing techniques: a literature review," *Computerized Medical Imaging and Graphics*, vol. 78, p. 101657, 2019.

[28] S. M. Pizer, E. P. Amburn, J. D. Austin et al., "Adaptive histogram equalization and its variations," *Computer vision, graphics, and image processing*, vol. 39, no. 3, pp. 355–368, 1987.

[29] S. Maheshwari, R. B. Pachori, and U. R. Acharya, "Automated diagnosis of glaucoma using empirical wavelet transform and correntropy features extracted from fundus images," *IEEE Journal of Biomedical and Health Informatics*, vol. 21, no. 3, pp. 803–813, 2017.

[30] T. R. Kausu, V. P. Gopi, K. A. Wahid, W. Doma, and S. I. Niwas, "Combination of clinical and multiresolution features for glaucoma detection and its classification using fundus images," *Biocybernetics and Biomedical Engineering*, vol. 38, no. 2, pp. 329–341, 2018.

[31] W. Zhou, Y. Yi, J. Bao, and W. Wang, "Adaptive weighted locality-constrained sparse coding for glaucoma diagnosis," *Medical & Biological Engineering & Computing*, vol. 57, no. 9, pp. 2055–2067, 2019.

[32] U. R. Acharya, S. Bhat, J. E. W. Koh, S. V. Bhandary, and H. Adeli, "A novel algorithm to detect glaucoma risk using texton and local configuration pattern features extracted from fundus images," *Computers in Biology and Medicine*, vol. 88, pp. 72–83, 2017.

[33] R. Bock, J. Meier, and G. Michelson, *Classifying Glaucoma with Image-Based Features from Fundus Photographs, in Proceedings of the Joint Pattern Recognition Symposium*, Springer, Berlin, Heidelberg, 2007.

[34] J. Nayak, U. Rajendra Acharya, P. S. Bhat, N. Shetty, and T.-C. Lim, "Automated diagnosis of glaucoma using digital fundus images," *Journal of Medical Systems*, vol. 33, no. 5, pp. 337–346, 2009.

[35] W. Zhou, H. Wu, C. Wu, X. Yu, and Y. Yi, "Automatic optic disc detection in color retinal images by local feature spectrum analysis," *Computational and Mathematical Methods in Medicine*, vol. 2018, 12 pages, 2018.

[36] W. Zhou and S. Qiao, "Automatic optic disc detection using low-rank representation based semi-supervised extreme learning machine," *Automatic optic disc detection using low-rank representation based semi-supervised extreme learning machine, in Proceedings of the International Journal of Machine Learning and Cybernetics*, vol. 11, no. 1, pp. 55–69, 2020.

[37] K. Zhou, S. Gao, and J. Cheng, "Sparse-Gan: sparsity-constrained generative adversarial network for anomaly detection in retinal oct image," in *in Proceedings of the 17th International Symposium on Biomedical Imaging (ISBI)*, pp. 1227–1231, IEEE, 2020.

[38] V. G. Edupuganti, A. Chawla, and A. Kale, "Automatic optic disk and cup segmentation of fundus images using deep learn-

ing," in *in Proceedings of the 25th IEEE International Conference on Image Processing (ICIP)*, pp. 2227–2231, IEEE, 2018.

[39] S. Yu, S. F. Di Xiao, and Y. Kanagasingam, "Robust optic disc and cup segmentation with deep learning for glaucoma detection," *Computerized Medical Imaging and Graphics*, vol. 74, pp. 61–71, 2019.

[40] S. Wang, L. Yu, X. Yang, C.-W. Fu, and P.-A. Heng, "Patch-based output space adversarial learning for joint optic disc and cup segmentation," *IEEE Transactions on Medical Imaging*, vol. 38, no. 11, pp. 2485–2495, 2019.

[41] H.-K. Hsiao, C.-C. Liu, C.-Y. Yu, S.-W. Kuo, and S.-S. Yu, "A novel optic disc detection scheme on retinal images," *Expert Systems with Applications*, vol. 39, no. 12, pp. 10600–10606, 2012.

[42] E. F. Kao, P. C. Lin, and M. C. Chou, "Automated detection of fovea in fundus images based on vessel-free zone and adaptive Gaussian template," *Computer Methods and Programs in Biomedicine*, vol. 117, no. 2, pp. 92–103, 2014.

[43] P. K. Chaudhary and R. B. Pachori, "Automatic diagnosis of glaucoma using two-dimensional Fourier-Bessel series expansion based empirical wavelet transform," *Biomedical Signal Processing and Control*, vol. 64, p. 102237, 2021.

[44] J. Gilles, G. Tran, and S. Osher, "2D empirical transforms. Wavelets, ridgelets, and curvelets revisited," *SIAM Journal on Imaging Sciences*, vol. 7, no. 1, pp. 157–186, 2014.

[45] R. M. Haralick, K. Shanmugam, and I. H. Dinstein, "Textural features for image classification," *IEEE Transactions on systems, man, and cybernetics*, vol. SMC-3, no. 6, pp. 610–621, 1973.

[46] M. Mercimek and K. Gulez, "Real object recognition using moment invariants," *sadhana*, vol. 30, no. 6, pp. 765–775, 2005.

[47] S. A. Valle, W. Li, and S. J. Qin, "Selection of the number of principal components: the variance of the reconstruction error criterion with a comparison to other methods," *Industrial & Engineering Chemistry Research*, vol. 38, no. 11, pp. 4389–4401, 1999.

[48] I. T. Jolliffe and T. M. Uddin, "A modified principal component technique based on the LASSO," *Journal of Computational and Graphical Statistics*, vol. 12, no. 3, pp. 531–547, 2003.

[49] B. Efron, T. Hastie, and J. R. Tibshirani, "Least angle regression," *Annals of Statistics*, vol. 32, no. 2, pp. 407–451, 2004.

[50] J. I. Orlando, H. Fu, J. B. Breda et al., "Refuge challenge: a unified framework for evaluating automated methods for glaucoma assessment from fundus photographs," *Medical Image Analysis*, vol. 59, p. 101570, 2020.

[51] F. Fumero, S. Alayon, J. L. Sanchez, J. Sigut, and M. Gonzalez-Hernandez, "RIM-ONE: an open retinal image database for optic nerve evaluation," in *in: Proceedings of the 24th International Symposium on Computer-Based Medical Systems (CBMS)*, pp. 1–6, IEEE, Bristol, UK, 2011.

[52] S. Dua, U. R. Acharya, and P. Chowriappa, "Wavelet-based energy features for glaucomatous image classification," *IEEE Transactions on Information Technology in Biomedicine*, vol. 16, no. 1, pp. 80–87, 2012.

[53] J. Cheng, J. Liu, Y. Xu et al., "Superpixel classification based optic disc and optic cup segmentation for glaucoma screening," *IEEE Transactions on Medical Imaging*, vol. 32, no. 6, pp. 1019–1032, 2013.

[54] E. Santos, R. Veras, and M. Frazao, "A semiautomatic super-pixel based approach to cup-to-disc ratio measurement," in *in: Proceedings of the 2018 IEEE Symposium on Computers and Communications (ISCC)*, pp. 00621–00626, IEEE, 2018.

[55] B. Liu, D. Pan, and H. Song, "Joint optic disc and cup segmentation based on densely connected depthwise separable convolution deep network," *BMC Medical Imaging*, vol. 21, no. 1, pp. 1–12, 2021.